

SELF-SIMILARITY OF PASSIVE SCALARS IN A DECELERATING JET

Dong-hyuk Shin

School of Engineering
University of Edinburgh
King's Buildings, Edinburgh, EH9 3DW, UK
D.Shin@ed.ac.uk

A. J. Aspden

School of Mechanical & Systems Engineering
Newcastle University
Stephenson Building, Newcastle upon Tyne, NE1 7RU, UK
andrew.aspden@ncl.ac.uk

Edward S. Richardson

Faculty of Engineering and the Environment
University of Southampton
Highfield Campus, Southampton, SO17 1BJ, UK
E.S.Richardson@ed.ac.uk

ABSTRACT

Scalar mixing is investigated in a decelerating turbulent round jet using direct numerical simulation. The mass fraction of jet fluid and the fluid residence time, measured by the mass-weighted age of the jet fluid, both exhibit self-similar radial profiles in statistically-stationary turbulent jets. Upon stopping the inflow, a deceleration wave passes through the jet, behind which a new self-similar state is observed for the two scalar variables. The self-similar state during the jet deceleration is different from that in the statistically-stationary jet. Opposite to its behaviour in the steady-state jet, the jet fluid mass fraction exhibits a linear increase with downstream distance in the decelerating jet, whereas the centreline mass-weighted age of jet fluid remains proportional to downstream distance. The dynamics of the scalar mixing in the transient self-similar state are discussed through analysis of the scalar transport budgets.

Introduction

Mixing processes in unsteady jets are relevant to a wide range of environmental, biological and industrial systems. Modulation of the jet flow rate affects the dynamics of mixing between the jet fluid and the ambient fluid, controlling both the overall rate of mixing and the spatial distribution of the mass fraction of the jet fluid over time. In addition to the jet fluid mass fraction distribution, the residence time of the jet fluid is relevant in many applications since the extent to which chemical, physical, or biological processes progress within a given system depends upon the residence time of the jet fluid.

Fuel injection in diesel engines is one important example where modulation of the fuel injection rate strongly affects the system performance in terms of heat release rate and pollution production: excessive mixing at the end of fuel injection can lead to incomplete combustion and to increased hydrocarbon emissions; whereas inadequate mixing can also increase emission of particulate matter. Due to the difficulties of in-cylinder measurements and high-fidelity simulations of mixing and reaction processes in combustion engines, sound fundamental understanding of the effects of jet flow rate modulation on mixing dynamics is essential to the design process of compression-ignition engines. In that context, recent development of one-dimensional modelling for fuel jet dynamics (Knox & Genzale, 2016; Desantes *et al.*, 2009; Pastor *et al.*, 2015) has provided valuable insight concerning the influence of the injection profile on flow, mixing and chemical dynamics in diesel engines. These one-dimensional models effectively employ an assumption

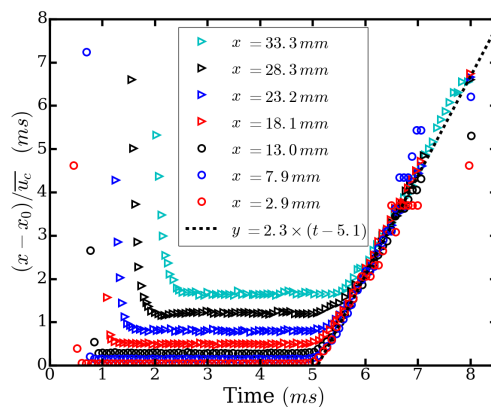


Figure 1. The scaled axial velocities along the centreline over time at different downstream locations, measured by Witze (1983). The air was injected between $t \approx 0.5 - 4.5$ ms.

that the velocity and jet fluid mass fraction exhibit a self-similar behaviour even during injection transients. However there is a lack of direct evidence for the occurrence of self-similarity of scalar fields during injection transients, and a lack of information concerning the form that such self-similarity takes.

A previous numerical study revealed that when a jet is stopped from a steady state, all the velocity components become self-similar, and the centreline streamwise velocity (\bar{u}_c) satisfies the following relationship with a constant C_u (Shin *et al.*, 2017a).

$$\bar{u}_c = C_u \frac{x - x_0}{t - t_0}, \quad (1)$$

where x_0 and t_0 are virtual space and time origins. This scaling behaviour agrees well with the experimental measurements of Witze (1983): Figure 1 shows that after the injection is stopped at around 4.5 ms, the inverse of scaled centreline velocities at different locations collapse onto a single straight line. This generic scaling is also identified by previous studies including Scase *et al.* (2006), Musculus (2009) and Craske & van Reeuwijk (2015).

The distribution of the jet fluid residence time provides additional information that may be used to enhance modelling of chemical processes, for example in one-dimensional models for diesel

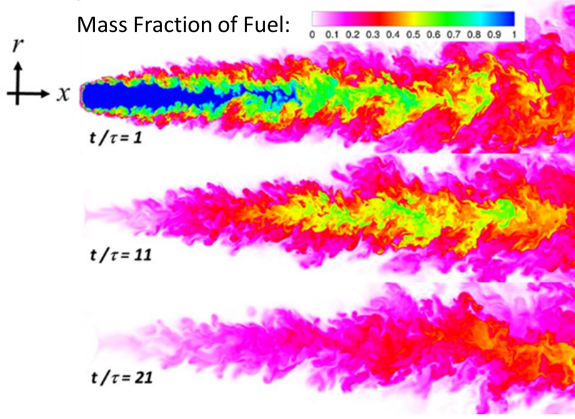


Figure 2. Cross-sectional colour maps of the instantaneous jet fluid mass fraction at $t/\tau = 1, 11$ and 21 following stopping of the jet at $t/\tau = 0$.

jets. Shin *et al.* (2017b) showed the residence time distribution of fluid from the jet stream is statistically-stationary and that radial profiles of jet fluid residence time are self-similar downstream of a development region (Shin *et al.*, 2017b). The objective of this study is to investigate the existence and nature of self-similarity of the jet fluid mass fraction and the jet fluid residence time following stopping of a turbulent jet.

Simulation Set-up

The simulation configuration consists of a turbulent round jet issuing from a flat plate with jet Reynolds number 7 290 and Mach number 0.304. A statistically-stationary flow is established (Shin *et al.*, 2017b), and then the inlet velocity is set to zero abruptly at $t = 0$. The simulation runs until 69τ ($\tau = D/U_0$), where U_0 is the bulk velocity and D is the jet inlet diameter. Four statistically-independent realisations of the flow are simulated.

The simulation is performed with the compressible DNS code, HipSTAR, developed at the University of Southampton (Sandberg & Tester, 2016). The simulation runs on a stretched cylindrical structured grid, with axial extent $x/D = 60$ and radial extent $r/D = 30$. Fourth-order finite differencing is used for the stream-wise and radial directions, and the spectral method is used for the circumferential direction.

The radial and downstream boundaries use Navier-Stokes Characteristic Boundary Conditions with buffer layers (Poinsot & Lele, 1992). All scalar diffusivities (\mathcal{D}) are set by assuming Lewis numbers equal to unity, and a Prandtl number equal to 0.72. Viscosity changes with temperature following Sutherland's Law Sutherland (1893). Figure 2 shows snapshots of mass fraction of jet fluid at $t/\tau = 1, 11$, and 21 .

In addition to the flow equations, two passive scalar transport equations are solved. The mass fraction of jet fluid (Z) and the 'stream age' of fluid material originating from the jet stream (a_j) are governed by the following equations (Ghirelli & Leckner, 2004):

$$\frac{\partial Z}{\partial t} + \bar{u} \cdot \nabla Z = \frac{1}{\rho} \nabla \cdot (\rho \mathcal{D}_j \nabla Z), \quad (2)$$

$$\frac{\partial (Za_j)}{\partial t} + \bar{u} \cdot \nabla (Za_j) = \frac{1}{\rho} \nabla \cdot (\rho \mathcal{D}_j \nabla (Za_j)) + Z, \quad (3)$$

where \mathcal{D}_j is the mass diffusivity of the jet fluid. The product of mass fraction and stream age, $\Phi = Za_j$ is referred to as the mass-weighted stream age (Shin *et al.*, 2017b). The equation for mass-

weighted stream age is used in preference to the equation for stream age since the stream age is not defined in the limit $Z \rightarrow 0$.

Theoretical Analysis

Self-similarity of scalar profiles within a decelerating jet implies a particular form for the centreline variation of the statistics of the scalar variables as well as certain relationships between variables. Before analysing the numerical results, we provide a theoretical analysis in order to set out key predictions that follow from an assumption of self-similar scalar profiles in the unsteady jet. The analysis begins by recasting Eqs. 2 and 3 into cylindrical coordinates, neglecting diffusion terms and ensemble averaging:

$$\frac{\partial \bar{Z}}{\partial t} + \bar{u} \frac{\partial \bar{Z}}{\partial x} + \bar{v} \frac{\partial \bar{Z}}{\partial r} = -\frac{1}{r} \frac{\partial r \bar{v}' Z'}{\partial r} - \frac{\partial \bar{u}' Z'}{\partial x} \quad (4)$$

$$\frac{\partial \bar{\Phi}}{\partial t} + \bar{u} \frac{\partial \bar{\Phi}}{\partial x} + \bar{v} \frac{\partial \bar{\Phi}}{\partial r} = -\frac{1}{r} \frac{\partial r \bar{v}' \Phi'}{\partial r} - \frac{\partial \bar{u}' \Phi'}{\partial x} + \bar{Z}, \quad (5)$$

where $(\bar{\cdot})$ denotes ensemble averaging.

The assumption of transient self-similarity for axial (u) and radial (v) velocities and all scalar variables can be expressed as follows:

$$\begin{aligned} \bar{u} &= \bar{u}_c(x, t) f_u(\eta), & \bar{v} &= \bar{u}_c(x, t) f_v(\eta), \\ \bar{Z} &= \bar{Z}_c(x, t) f_Z(\eta), & \bar{\Phi} &= \bar{\Phi}_c(x, t) f_\Phi(\eta), \\ \overline{u' Z'} &= \bar{u}_c(x, t) \bar{Z}_c(x, t) f_{uZ}(\eta), & \overline{v' Z'} &= \bar{u}_c(x, t) \bar{Z}_c(x, t) f_{vZ}(\eta), \\ \overline{u' \Phi'} &= \bar{u}_c(x, t) \bar{\Phi}_c(x, t) f_{u\Phi}(\eta), & \overline{v' \Phi'} &= \bar{u}_c(x, t) \bar{\Phi}_c(x, t) f_{v\Phi}(\eta), \end{aligned} \quad (6)$$

where $\eta = r/x$ and f_i represents the shape function for each variable i .

Mathematical manipulation (omitted for brevity) shows that the assumptions in Eq. 6 demand that \bar{Z}_c must be in the form

$$\bar{Z}_c = C_Z x^\alpha t^\beta, \quad (7)$$

where C_Z , α and β are constants. The two constants, α and β are not yet determined. Assuming that the mass fraction behaves similarly to the axial velocity, the constants corresponding to Eq. 1 are $\alpha = 1$ and $\beta = -1$. With these parameters, the centreline evolution of the two scalars is given by:

$$\bar{Z}_c = C_Z \frac{x - x_0}{t - t_0}, \quad (8)$$

$$\bar{\Phi}_c = C_\Phi (x - x_0), \quad (9)$$

where C_Φ is a constant. Substituting Eqs. 1, 6, 8, and 9 into Eqs. 4 and 5, and normalising by $C_u x/t^2$ and $C_u x/t$ respectively, the governing equations are expressed in terms of η as follows:

$$\begin{aligned} -\frac{1}{C_u} f_Z + f_u f_Z - \eta f_u \frac{df_Z}{d\eta} + f_v \frac{df_Z}{d\eta} \\ = -\left[\frac{f_v Z}{\eta} + \frac{df_v Z}{d\eta} \right] - \left[2f_u Z - \eta \frac{df_u Z}{d\eta} \right], \end{aligned} \quad (10)$$

$$\begin{aligned} f_u f_\Phi - \eta f_u \frac{df_\Phi}{d\eta} + f_v \frac{df_\Phi}{d\eta} \\ = -\left[\frac{f_v \Phi}{\eta} + \frac{df_v \Phi}{d\eta} \right] - \left[2f_u \Phi - \eta \frac{df_u \Phi}{d\eta} \right] + \frac{C_Z}{C_u C_\Phi} f_Z, \end{aligned} \quad (11)$$

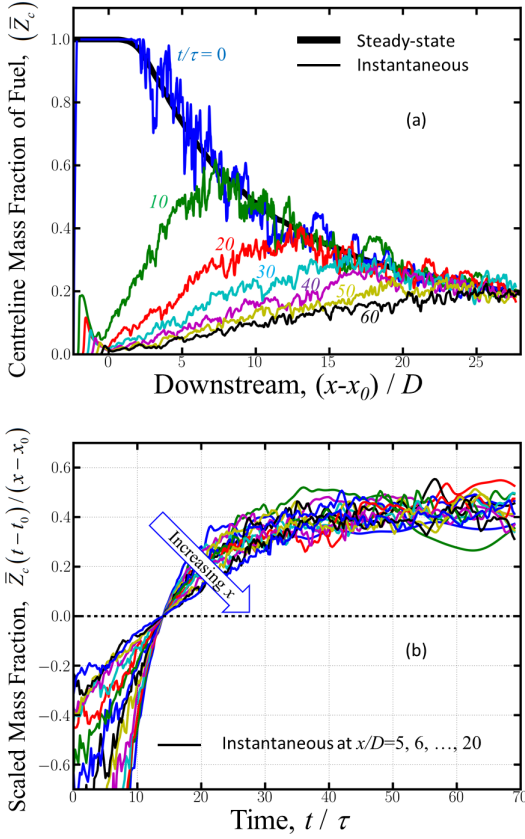


Figure 3. (a) Time evolution of the mass fraction of jet fluid along the centreline (\bar{Z}_c), and (b) the scaled mass fraction of jet fluid along the centreline ($\bar{Z}_c(t-t_0)/(x-x_0)$) at selected locations over time.

which reduces the original partial differential equations into ordinary differential equations in η .

Evaluating Eqs. 10 and 11 at $\eta = 0$ leads:

$$\left[\frac{df_{vZ}}{d\eta} \right]_{\eta=0} = \frac{1}{2C_u} - \frac{1}{2} - f_{uZ}(0), \quad (12)$$

$$\left[\frac{df_{v\Phi}}{d\eta} \right]_{\eta=0} = \frac{C_Z}{2C_u C_\Phi} - \frac{1}{2} - f_{u\Phi}(0), \quad (13)$$

which provides simple relationships for the slopes of f_{vZ} and $f_{v\Phi}$ at $\eta = 0$.

Results

Centreline variation

The DNS data is used to investigate how the centreline profiles vary in the decelerating jet and to assess the validity of Eqs. 8 and 9. Figure 3a shows instantaneous profiles of jet fluid mass fraction (\bar{Z}_c) along the centreline. For reference, the averaged steady-state profile is added as a thick solid line. The transient behaviour of \bar{Z}_c is very similar to the centreline axial velocity (Shin *et al.*, 2017a). Once the jet inflow is arrested, a deceleration wave travels downstream at close to the local centreline velocity (Musculus, 2009; Shin *et al.*, 2017a; Scase *et al.*, 2006). Upstream of the deceleration wave the jet fluid mass fraction decays over time and develops a linear dependence on x with the gradient decreasing in time, in accordance with Eq. 8. Downstream of the deceleration wave the flow field and scalar profiles are yet to be affected by the deceleration, and resemble the profiles in the steady-state jet.

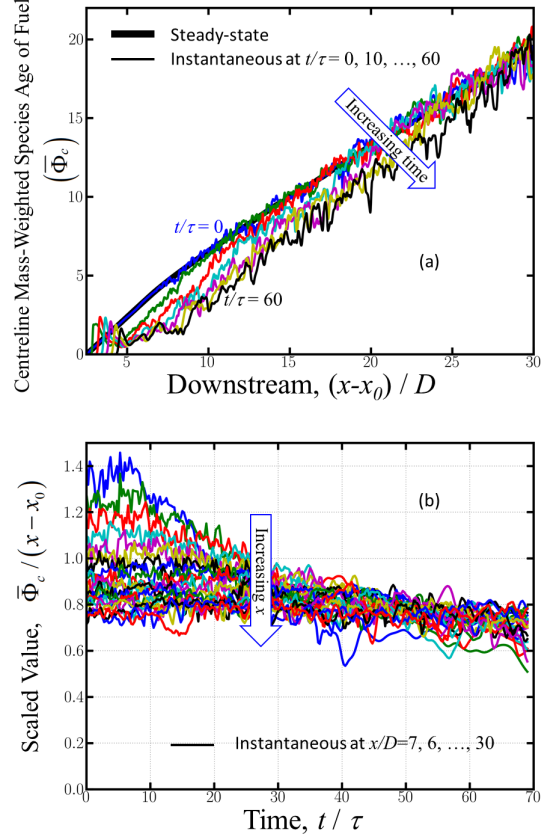


Figure 4. (a) Time evolution of the mass-weighted stream age of jet fluid along the centerline ($\bar{\Phi}_c$), and (b) the scaled mass-weighted stream age of jet fluid ($\bar{\Phi}_c/(x-x_0)$) at selected locations over time.

To further validate the scaling in Eq. 8, the scaled \bar{Z}_c is plotted in Figure 3b. For consistency with previous work Shin *et al.* (2017a), the virtual origin x_0 and reference time t_0 are obtained respectively by fitting the steady-state axial velocity profile and by fitting Eq. 1 against the data for \bar{u}_c in the decelerating jet. The figure shows that the scaled \bar{Z}_c asymptotes to a constant after a transition period. Due to the finite speed of the deceleration wave, the transition period increases with the axial position. This asymptotic behaviour confirms the agreement with Eq. 8, and the asymptotic constant, C_Z , is found to be approximately 0.41.

Next, Figure 4a shows profiles of the instantaneous mass-weighted species age of jet fluid ($\bar{\Phi}_c$) along the centreline, and the ensemble average of $\bar{\Phi}_c$ from the steady-state jet simulation (Shin *et al.*, 2017b). In contrast with the behaviour of \bar{Z}_c , the $\bar{\Phi}_c$ profile changes relatively little as the jet decelerates. As the deceleration wave passes through the jet, $\bar{\Phi}_c$ transitions from an initial linear dependence on axial location in the steady-state jet to a different time-independent linear profile with a slightly greater gradient. This behaviour is consistent with Eq. 9. Figure 4b shows the scaled $\bar{\Phi}_c$ over time at multiple downstream locations. Using the same virtual origin x_0 in the scaling, the figure shows that the scaled $\bar{\Phi}_c$ asymptotes towards 0.73 after the deceleration wave passes.

The asymptotic behaviour of the scaled centreline values shown in Figures 3b and 4b agrees with Eqs. 8 and 9, indicating that the DNS data are consistent with the self-similar assumptions underpinning Eqs. 8 and 9.

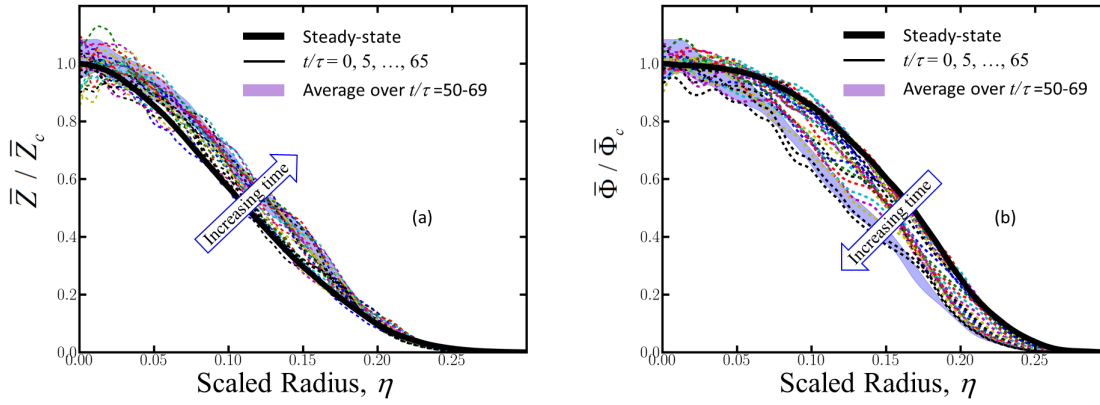


Figure 5. Time evolutions of the radial profiles of (a) the scaled mass fraction of jet fluid (Z) at $x/D = 15$, and (b) the scaled mass-weighted stream age of jet fluid (Φ) at $x/D = 15$.

Self-similar radial profiles

The evolution of the radial profiles of \bar{Z} and $\bar{\Phi}$ during the deceleration transient is shown for $x/D = 15$ in Fig. 5a and b respectively. The figures show an ensemble average of the profiles in the initial steady-state jet, instantaneous profiles during the jet deceleration, and an average of profiles during the period $t/\tau = 50 - 69$. The time range $t/\tau = 50 - 69$ refers to a period after the passage of the deceleration wave once the centreline velocity, mass fraction and mass-weighted stream age evolve according to Eqs. 1, 8 and 9 (Shin *et al.*, 2017a). \bar{Z} and $\bar{\Phi}$ are normalised by smoothed centreline values, with the smoothed centreline values obtained by fitting a sixth-order polynomial to the data.

Figure 5a shows that the radial profile of \bar{Z} evolves from the steady-state jet profile towards a new time-independent profile following the passage of the deceleration wave. The profile in the decelerating jet is similar to, but slightly wider than, the profile in the steady-state jet. The difference between the steady-state profile and the profile in the decelerating jet is similar to the difference in the axial-velocity profile (Borée *et al.*, 1996; Shin *et al.*, 2017a). The radial profile of $\bar{\Phi}$ also transitions from its steady-state jet profile to a new time-independent profile. In contrast with the jet fluid mass fraction profile, the profile of $\bar{\Phi}$ becomes narrower during the deceleration wave.

While the transient profiles and the steady-state profiles of the passive scalars are not identical to each other, they are quite similar. Therefore, for some purposes, it may be justifiable to assume that the steady-state profile does not change during the deceleration wave. For example, Musculus (2009) obtained good predictions of the axial velocity evolution in a decelerating transient turbulent jet by assuming a constant self-similar velocity profile.

The same transition to time-independent radial profiles of \bar{Z}/\bar{Z}_c and $\bar{\Phi}/\bar{\Phi}_c$ in the decelerating jet is observed for x -locations downstream of a development region, $x/D > 12.5$ (not shown). Furthermore, the radial profiles of \bar{Z}/\bar{Z}_c and $\bar{\Phi}/\bar{\Phi}_c$ in the decelerating jet are independent of axial location – implying that the radial profiles in the decelerating jet achieve a new self-similar state after the transit of the deceleration wave. This self-similarity is evident in the axial region for which the jet is fully-developed and for which sufficiently statistically-converged data are available ($12.5 < x/D < 20$).

Figures 6a-d show the profiles of the turbulent transport terms arising in the averaged scalar transport equations, Eqs. 4 and 5. Each figure shows the initial self-similar profiles in the steady-state jet and the new self-similar profile given by averaging data over $x/D = 12.5 - 20$ and $t/\tau = 50 - 69$, as well as showing the standard deviation in the data from the decelerating jet. Although not

shown, \bar{Z}/\bar{Z}_c and $\bar{\Phi}/\bar{\Phi}_c$ have very narrow standard deviations when averaged in this way, indicating that profiles in the decelerating jet are self-similar with respect to time and axial location. However, a larger standard deviation is expected for the terms involving second moments.

Figure 6a shows the radial profiles of $\overline{u'Z'}$. Both profiles have similar centreline values ($\eta = 0$): $\overline{u'Z'} = 0.01$ for steady-state and 0.013 for the decelerating jet. The peak occurs at different locations: $\eta = 0.06$ for the steady-state and 0.13 for the unsteady. Then, both drop to zero at the same η location, indicating the jet width does not change during the deceleration.

The $\overline{v'Z'}$ profiles are shown in Figure 6c. The peak locations are slightly different ($\eta = 0.07$ for the steady-state and $\eta = 0.10$ for the decelerating jet), however the difference in locations of the peak follows a similar trend as for $\overline{u'Z'}$. To further assess the validity of the self-similar assumption, the $\overline{v'Z'}$ gradient at $\eta = 0$ predicted by Eq. 12 is plotted. Considering $C_u = 0.455$ and $f_{uZ}(0) = 0.013$, the theoretical analysis in Eq. 12 predicts the slope of $\overline{v'Z'}$ to be 0.584, which agrees well with the simulation data.

Figure 6b shows the $\overline{u'\Phi'}$ profiles. Interestingly, the decelerating jet profiles for $\overline{u'Z'}$ and $\overline{u'\Phi'}$ have the same shape, whereas their steady-state counterparts are different. This may be because the fluctuation a'_j becomes relatively small, so that Φ' is dominated the Z' fluctuation. The centreline value of the $\overline{u'\Phi'}$ in the decelerating jet has a non-zero value, whereas it is zero in the steady-state jet. However the difference may not be statistically significant considering the standard deviation in the data.

Figure 6d shows the $\overline{v'\Phi'}$ profiles. The peak locations are quite close each other: $\eta = 0.145$ for steady-state and $\eta = 0.13$ for the unsteady. The closeness of the peak location is similar to $\overline{u'\Phi'}$ profiles. In the Theoretical Analysis section the initial slope is predicted by Eq. 13. Given the constants of $C_u = 0.455$, $C_Z = 0.41$, and $C_\Phi = 0.73$, the slope is expected to be 0.12 (red dashed line). However, this prediction does not agree with the numerical data. This discrepancy may be due to a not-fully converged value for C_Φ . As seen from Figure 4b, the scaled $\bar{\Phi}_c$ continues to decrease gradually. If C_Φ is set to be 0.51 instead of 0.73, the slope matches better. Also, the large standard deviation in the data prevents an accurate comparison.

Scalar transport budgets

Once all the necessary self-similar profiles have been evaluated, all terms in Eqs. 4 and 5 can be evaluated to compare their relative contributions and to examine effect of the approximations

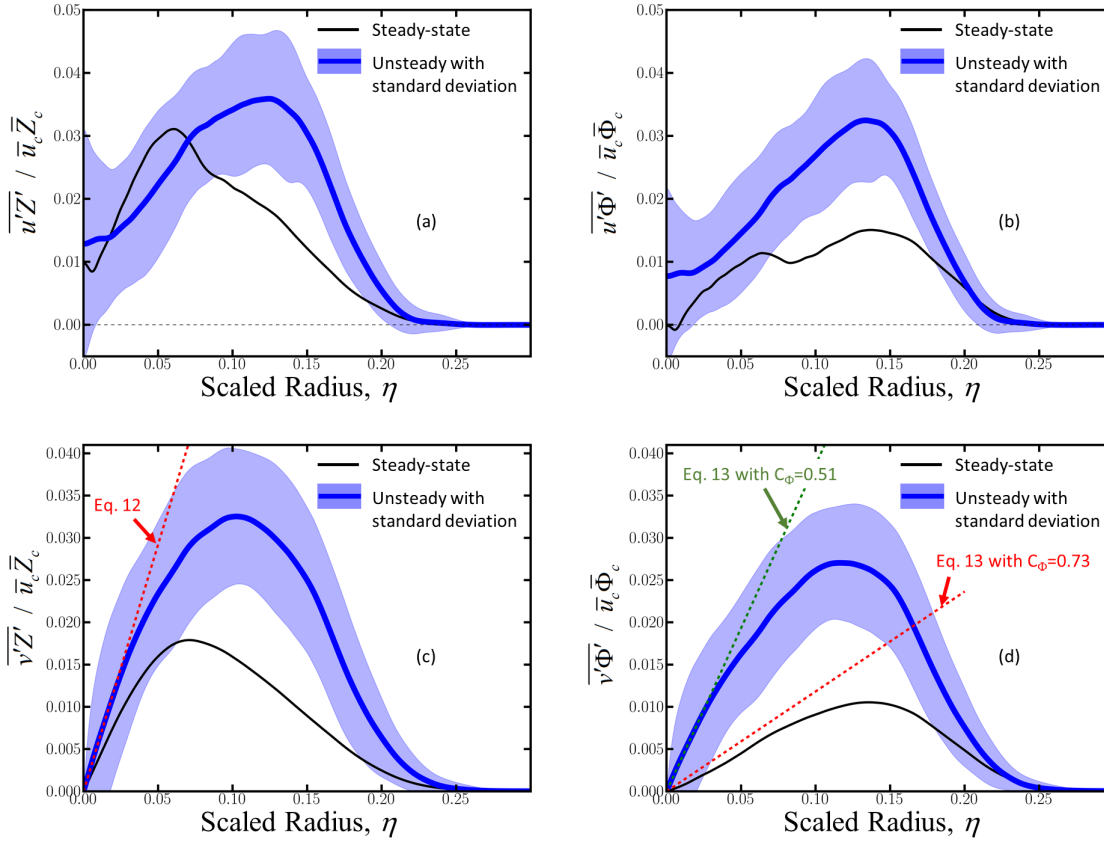


Figure 6. Self-similar radial profiles for a decelerating jet of (a) $\overline{u'Z'}$, (b) $\overline{u'\Phi'}$, (c) $\overline{v'Z'}$, (d) $\overline{v'\Phi'}$. Each figure contains: the unsteady self-similar profile in a thick blue line with the shade of standard deviation; a corresponding steady-state profile in a black solid line and; theoretical predictions in dashed lines if possible.

in Eqs. 4 and 5.

Figures 7a-d show the budget terms of the scalar transport equations Eqs. 4 and 5 for both the steady-state and the decelerating jet (based on data from $x/D = 12.5 - 20$ and $t/\tau = 50 - 69$). All the terms are scaled in order to be expressed in terms of η – for example giving Eqs. 10 and 11 are for unsteady conditions. In addition, for ease of comparison, all values are re-scaled in a way such that the axial transport term ($u\partial(\cdot)/\partial x$) has unity magnitude at $\eta = 0$.

The \bar{Z} -budget terms for the decelerating jet are shown in 7a. Four terms are significant: axial transport, radial transport, radial turbulent transport, and temporal terms. The temporal term makes the biggest contribution. When compared with the steady-state jet data shown in Figure 7b, the axial transport and the radial turbulent transport terms have a similar order of magnitude in the steady-state and the decelerating jets. The axial transport terms are positive for unsteady while negative for steady-state because of the different x -dependency of \bar{Z} . Interestingly, the radial transport term becomes larger, relative to the steady-state jet. This is because the normalised radial velocity (i.e. the entrainment) becomes around three times larger in the decelerating jet (Shin *et al.*, 2017a). The balance term slightly deviates from zero, and this may be due to incompletely converged averaging.

Figure 7c shows the budget-terms of $\bar{\Phi}$ for the decelerating jet. Four terms are important: axial transport, radial transport, radial turbulent, and the source term ($-\bar{Z}$). The source term in Eq. 11 is evaluated assuming $C_\Phi = 0.51$. The value of $C_\Phi = 0.51$ is chosen in order to match the slope of $v'\Phi'$ at $\eta = 0$ in Fig. 6d. If $C_\Phi = 0.73$ is used instead, the source term ($-\bar{Z}$) would be smaller in magnitude

by a factor of 1.43, and the balance term is more positive accordingly. No other terms are affected by the choice of C_Φ . When compared with the steady-state condition in Figure 7d, axial transport terms are quite similar, while the radial turbulent term magnitude increases due to the greater entrainment in the decelerating jet.

The analysis of the scalar transport budgets shows that the radial convection term becomes significant in the decelerating jet due to the three-fold increase in entrainment. The unsteady term is the leading order term in the \bar{Z} budget in the decelerating jet, whereas it is negligible (part of the Balance) in the $\bar{\Phi}$ budget. The near-zero balances in both cases indicate that the reduced ordinary differential equations in Eqs. 10 and 11 are valid, although uncertainty concerning the value of C_Φ needs to be resolved.

CONCLUSION

Scalar mixing is investigated in a decelerating turbulent round jet using direct numerical simulation. It is found that the mass fraction of jet fluid and the mass-weighted stream age of the jet fluid both exhibit self-similar radial profiles in the decelerating jet as well as in the statistically-stationary jet. The self-similar profiles of the averaged scalar variables differ between the steady-state and decelerating jets, however the differences are relatively small and it might be a reasonable approximation to use radial profiles from steady-state jets in some modelling applications. A deceleration wave passes through the flow as the jet decelerates. Behind the deceleration wave the jet fluid mass fraction exhibits a linear increase with downstream distance, opposite to the mass fraction dependence in the steady-state jet. In contrast, the centreline profile of mass-weighted stream age remains proportional to downstream

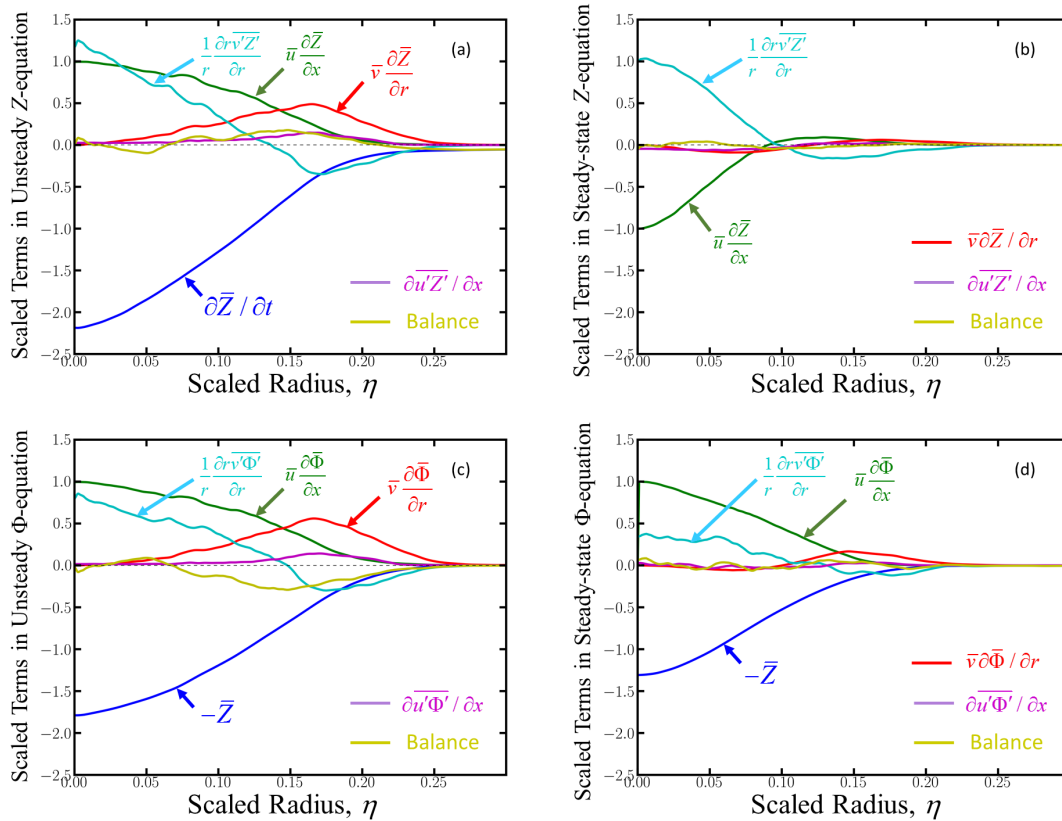


Figure 7. Budget terms of (a) mass fraction of jet fluid (Z) of unsteady, (b) Z of steady-state, (c) mass-weighted stream age of jet fluid (Φ) of unsteady, and (d) Φ of steady-state,

distance, with a slight change of the gradient, and becomes independent of time. The assumption of transient self-similarity of the scalar fields in the decelerating jet leads to theoretical predictions concerning the form of the turbulent scalar fluxes, and these predictions are consistent with the simulation data – providing further evidence for self-similarity of the scalar fields in the decelerating jet. The transport budgets for the averaged jet fluid mass fraction and mass-weighted stream age show marked differences in the decelerating jet, compared to the steady-state jet. In particular the entrainment is around three times greater in the decelerating jet, promoting the importance of radial convection. Remarkably, the unsteady term is negligible in the mass-weighted stream age budget in the decelerating jet, so that the averaged mass-weighted stream age distribution returns to a statistically stationary state after the deceleration wave has passed, even though the flow continues to decelerate.

Acknowledgment

This work has been performed with support from the EPSRC EP/L002698/1 and EPSRC EP/M001482/1.

REFERENCES

Borée, J, Atassi, N & Charnay, G 1996 Phase averaged velocity field in an axisymmetric jet subject to a sudden velocity decrease. *Experiments in fluids* **21** (6), 447–456.

Craske, John & van Reeuwijk, Maarten 2015 Energy dispersion in turbulent jets. Part1. Directsimulation of steady and unsteady jets. *Journal of Fluid Mechanics* **763**, 500–537.

Desantes, J.M., Pastor, J.V., Garca-Oliver, J.M. & Pastor, J.M. 2009 A 1d model for the description of mixing-controlled reacting diesel sprays. *Combustion and Flame* **156** (1), 234 – 249.

Ghirelli, F & Leckner, B 2004 Transport equation for the local resi-

dence time of a fluid. *Chemical Engineering Science* **59** (3), 513–523.

Knox, Benjamin W & Genzale, Caroline L 2016 Reduced-order numerical model for transient reacting diesel sprays with detailed kinetics. *International Journal of Engine Research* **17** (3), 261–279.

Musculus, Mark P. B. 2009 Entrainment waves in decelerating transient turbulent jets. *Journal of Fluid Mechanics* **638** (1), 117.

Pastor, Jose V., Garcia-Oliver, Jose M., Pastor, Jose M. & Vera-Tudela, W. 2015 One-dimensional diesel spray modeling of multicomponent fuels. *Atomization and Sprays* **25** (6), 485–517.

Poinsot, T. J. & Lele, S.K. 1992 Boundary conditions for direct simulations of compressible viscous flows. *Journal of Computational Physics* **101** (1), 104–129.

Sandberg, R. D. & Tester, B. J. 2016 Mach-number scaling of individual azimuthal modes of subsonic co-flowing jets. *Journal of Fluid Mechanics* **793**, 209–228.

Scase, MM, Caulfield, CP, Dalziel, SB & Hunt, JCR 2006 Time-dependent plumes and jets with decreasing source strengths. *Journal of Fluid Mechanics* **563**, 443–461.

Shin, Dong-hyuk, Aspden, Andy & Richardson, Edward S 2017a Self-similar decelerating turbulent round jet. *Journal of Fluid Mechanics, under preparation* .

Shin, Dong Hyuk, Sandberg, Richard & Richardson, Edward 2017b Self-similarity of fluid residence time statistics in a turbulent round jet. *Journal of Fluid Mechanics, under review* .

Sutherland, W. 1893 Lii. the viscosity of gases and molecular force. *Philosophical Magazine Series 5* **36** (223), 507–531.

Witze, Peter O 1983 Hot-film anemometer measurements in a starting turbulent jet. *AIAA Journal* **21** (2), 308–309.